Mechanics of Advanced Materials and Structures, 14:227–244, 2007

ISSN: 1537-6494 print / 1537-6532 online
DOI: 10.1080/15376490600790221

Taylor & Francis
Taylor & Francis Group

On Fracture Criteria for Mixed-Mode Crack Propagation in Functionally Graded Materials

Jeong-Ho Kim
Department of Civil and Environmental Engineering, University of Connecticut, Storrs, Connecticut, USA

Glaucio H. Paulino
Department of Civil and Environmental Engineering, University of Illinois at Urbana-Champaign, Newmark Laboratory, Urbana, Illinois, USA

This paper addresses mixed-mode crack growth in two-dimensional functionally graded materials, and assesses the predictive capability of some fracture criteria on both crack growth direction and crack initiation condition. Automatic simulation of mixed-mode crack propagation in homogeneous and functionally graded materials is performed by means of the finite element method in conjunction with a remeshing algorithm. Crack growth simulation consists of iterative procedures for the calculation of mixed-mode stress intensity factors by means of the interaction integral method, determination of crack growth direction and crack initiation, and local automatic remeshing along the crack path. The present approach requires a user-defined crack increment at the beginning of the simulation. Crack trajectories obtained by the present simulation are compared with available experimental results.

Keywords functionally graded material (FGM), interaction integral method, finite element method (FEM), crack propagation, fracture criteria, remeshing algorithm.

1. INTRODUCTION

Functionally graded materials (FGMs) are multifunctional composites involving spatially varying volume fractions of constituent materials, thus providing a graded microstructure, macroproperties [1–4]. Recently, FGMs have been applied to many applications: thermal barrier coatings [5, 6]; first-wall composites in nuclear fusion and fast breeder reactors [7]; piezoelectric and thermoelectric devices, and high-density magnetic recording media and position-measuring devices [8–11]; graded refractive index materials [12]; thermionic converters [13]; dental and other implants [14–17]; fire retardant doors [18]; solid oxide fuel cells [19, 20] and other applications [2, 3].

Received 5 January 2006; accepted 18 April 2006.
Address correspondence to Glaucio H. Paulino, Department of Civil and Environmental Engineering, University of Illinois at Urbana-Champaign, Newmark Laboratory, 205 North Mathews Ave., Urbana, IL 61801. E-mail: paulino@uiuc.edu

Due to multifunctional capabilities, FGMs have been investigated for various damage and failure mechanisms under mechanical or thermal loads, and static, dynamic or fatigue loads, etc. Lin et al. [21] investigated mode I fracture of aluminium alloy 2124/SiC FGMs considering a crack parallel to the material gradation. Carpenter et al. [22] performed fracture testing and analysis of a layered functionally graded Ti/TiB beam subjected to three-point bending. Rousseau and Tippur [23] performed experimental and numerical investigations on crack growth in an epoxy/glass FGM beam subjected to four-point bending. Lambros et al. [24] and Abanto-Bueno and Lambros [25] investigated mode I crack growth in FGMs subjected to fixed-grip loading. Their FGMs were fabricated by selective controlled ultraviolet (UV) irradiation on ethylene carbon monoxide co-polymer (ECO). Jin et al. [26, 27] investigated elastic-plastic mode I crack growth in TiB/Ti FGMs by using three-dimensional interface cohesive elements. Kim and Paulino investigated two-dimensional mixed-mode crack propagation in FGMs using the finite element method and interaction integrals and also considered non-proportional loading [28]. Zhang and Paulino used cohesive zone models to simulate two-dimensional mixed-mode dynamic crack propagation in FGMs [29]. Moon et al. [30] investigated crack growth resistance (R-curve) behavior of multilayer graded alumina-zirconia FGMs considering a crack parallel to the material gradation. Neubrand [31] performed experimental and theoretical investigations on the R-curve for Al/Al_2O_2 FGMs under mechanical loading. Fujimoto and Noda [32] investigated propagation of a single crack in a partially stabilized zirconia (PSZ) and T1-6A1-4V FGMs under transient thermal loads. Noda et al. [33] extended the investigation to two interacting edge cracks in FGMs. Uzun et al. [34] investigated fatigue crack growth of 2124/SiC/l0p single-core bulk FGMs considering mechanical loading. Forth et al. [35] investigated three-dimensional mixed-mode fatigue crack growth behavior of Ti-6A1-4V β-STOA FGM considering mechanical loadings.

This paper focuses on two-dimensional mixed-mode crack propagation in FGMs using the finite element method (FEM)

with mesh refinement techniques, and compares the performance of some fracture criteria in predicting crack trajectory and crack initiation conditions for cracked FGMs. Local homogenization around the crack-tip region in FGMs allows one to adopt existing fracture criteria, which have been widely used for homogeneous materials. Such criteria include the maximum hoop stress criterion [36], the maximum energy release rate criterion [37, 38], the minimum strain energy density criterion [39], the $K_{II} = 0$ criterion [40], the so-called T-criterion (extension of minimum strain energy density criterion) [41], the maximum stress triaxiality criterion [42], the W-criterion ($W = r_p/a$, the ratio of plastic zone boundary size to half crack length) [43, 44], and the R-criterion ($R = r_p/[a(\sigma/\sigma_{\rm YS})^2]$ is a non-dimensional elastic-plastic core region radius where σ denotes stress and σ_{YS} denotes the yield stress of the material) [45]. In this paper, we use and compare the first three fracture criteria.

The present approach uses a user-defined crack increment, and it is provided at the beginning of each step. For homogeneous materials, Hori and Vaikuntan [46] proposed a formulation to determine the curvature and length of a small crack extension, and Fortino and Bilotta [47] proposed an algorithm to evaluate the amount of crack growth based on the coupled displacement-crack propagation rate problem. Integrated theoretical and experimental investigation on a crack increment in FGMs (and other materials) is needed, but it is beyond the scope of the present work.

This paper is organized as follows. Section 2 presents selected fracture criteria. Section 3 explains strategy for automatic crack propagation in FGMs. Section 4 presents the interaction integral method for evaluating mixed-mode stress intensity factors (SIFs). Section 5 provides some numerical examples.

Finally, Section 6 presents some conclusions of this work.

2. FRACTURE CRITERIA

The asymptotic stresses for a crack in linear elastic FGMs are given by (see Figure 1)

$$\begin{aligned}
\sigma_{rr} &= \frac{1}{\sqrt{2\pi r}}\cos\frac{\theta}{2}\left[K_I\left(1+\sin^2\frac{\theta}{2}\right)\right.\\
&\quad\left.+\frac{3}{2}K_{II}\left(\sin\theta-2\tan\frac{\theta}{2}\right)\right],\\
\sigma_{\theta\theta} &= \frac{1}{\sqrt{2\pi r}}\cos\frac{\theta}{2}\left[K_I\cos^2\frac{\theta}{2}-\frac{3}{2}K_{II}\sin\theta\right],\\
\sigma_{r\theta} &= \frac{1}{2\sqrt{2\pi r}}\cos\frac{\theta}{2}[K_I\sin\theta+K_{II}(3\cos\theta-1)],
\end{aligned} \tag{1}$$

where K_I and K_{II} denote mode I and II SIFs, respectively. The singularity ($r^{-1/2}$) and angular functions for FGMs are the same as for homogeneous materials, which provides a basis of local homogenization [48, 49]. Thus local homogenization allows the use of fracture criteria, which have been widely used for homogeneous materials (see Figure 2). Figure 3 shows a fracture

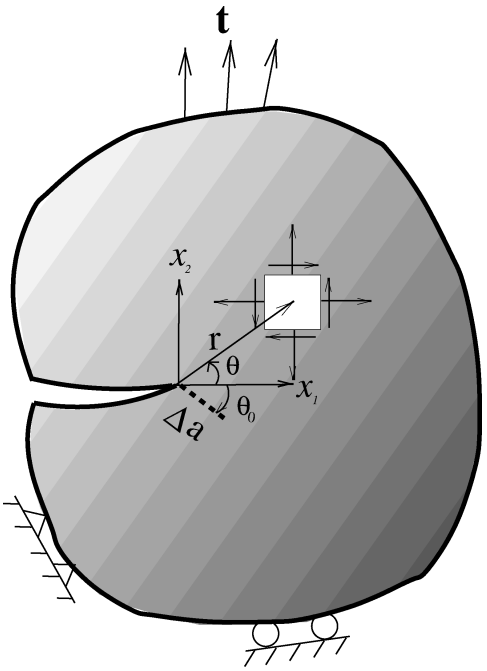

FIG. 1. Cartesian (x_1, x_2) and polar (r, θ) coordinates originating from the crack tip in a general FGM under traction (**t**) and displacement boundary conditions. The crack initiation angle is θ_0, and Δa denotes the crack extension.

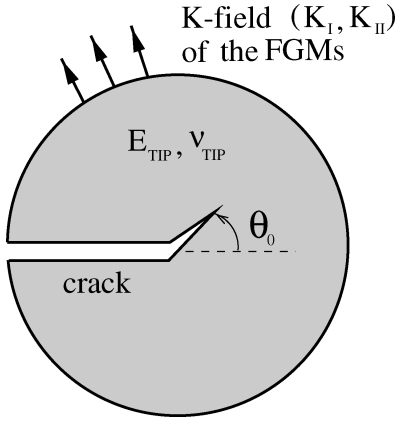

FIG. 2. Local homogenization [71] near the crack tip in an FGM. A locally homogenized material is subjected to the K-field of the crack in FGMs.

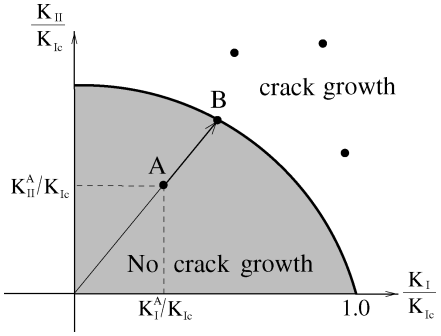

FIG. 3. Fracture locus involving mode I and II SIFs and fracture toughness K_{Ic}. Note that both K_I and K_{II} are normalized with respect to K_{Ic}.

locus involving mode I and II SIFs, and fracture toughness K_{Ic}. If the crack driving force is big enough for crack-tip fields to reach the fracture envelope, then the crack grows.

The fracture locus can be obtained by experiments, theoretical fracture criteria, or combination of both. In this paper, we focus on local homogenization-based theoretical fracture criteria such as the maximum hoop stress [36], the maximum energy release rate [37] and the minimum strain energy density [39] criteria. The three criteria are briefly reviewed below, with simple adaptations for nonhomogeneous materials and FGMs.

2.1. Maximum Hoop Stress

Erdogan and Sih [36] proposed the maximum hoop stress criterion. They postulated that the crack will grow in the direction along which the maximum hoop stress $\sigma_{\theta\theta}$ occurs (i.e., the shear stress $\sigma_{r\theta}$ is zero). Therefore the crack initiation angle θ_0 is obtained from

$$\partial\sigma_{\theta\theta}/\partial\theta = 0,\ \partial^2\sigma_{\theta\theta}/\partial\theta^2 < 0 \Rightarrow \theta = \theta_0. \tag{2}$$

Substitution of $\sigma_{\theta\theta}$ from Eq. (1) into Eq. (2) leads to [36]

$$\cos\frac{\theta_0}{2}[K_I \sin\theta_0 + K_{II}(3\cos\theta_0 - 1)] = 0 \tag{3}$$

Once the crack initiation angle is determined, the crack initiation condition is obtained as [36]

$$\sqrt{2\pi r}(\sigma_{\theta\theta}) = \cos\frac{\theta_0}{2}\left[K_I \cos^2\frac{\theta_0}{2} - \frac{3}{2}K_{II}\sin\theta_0\right]. \tag{4}$$

For pure mode I, when K_{II} and θ_0 are all equal to zero, K_I can be replaced by the mode I fracture toughness function $K_{Ic}(x)$. Therefore

$$\sqrt{2\pi r}(\sigma_{\theta\theta}) = K_{Ic}(x). \tag{5}$$

Substitution of Eq. (5) into Eq. (4) yields the crack initiation condition [36]:

$$\cos\frac{\theta_0}{2}\left[K_I \cos^2\frac{\theta_0}{2} - \frac{3}{2}K_{II}\sin\theta_0\right] = K_{Ic}(x). \tag{6}$$

2.2. Maximum Strain Energy Release Rate

Hussain et al. [37] proposed the maximum strain energy release rate criterion for homogeneous materials. They postulated that the crack subjected to combined loads will grow in the direction along which the strain energy release is maximum and the crack will start to grow when the maximum strain energy release rate reaches a critical value. The energy release rate for combined mode I and mode II loading in FGMs is given by

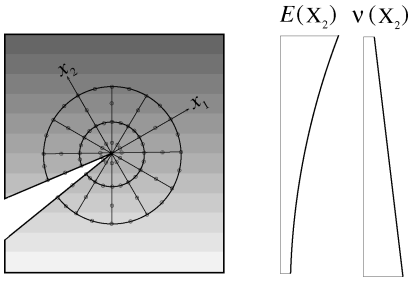

FIG. 4. Crack-tip discretization for a crack in a nonhomogeneous material.

$$\mathcal{G} = \frac{K_I^2 + K_{II}^2}{E^*_{\text{tip}}}, \tag{7}$$

where $E^*_{\text{tip}} = E_{\text{tip}}$ for plane stress and $E_{\text{tip}}/(1-\nu^*_{\text{tip}})$ for plane strain. Equation (7) is obtained by assuming that a crack under mixed-mode loading moves along its own plane. However, in general, the crack grows in a direction which is not parallel to its initial tangent plane. Hussain et al. [37] obtained an elasticity solution for a straight main crack and a branch crack extended at an arbitrary angle, and computed the energy release rate in the limit as the propagation branch vanishes. The energy release rate is given by [37]

$$\begin{aligned}\mathcal{G}(\theta) = \frac{4}{E^*_{\text{tip}}}&\left(\frac{1}{3+\cos^2\theta}\right)^2\left(\frac{1-\pi/\theta}{1+\pi/\theta}\right)^{\theta/\pi}\\ &\times\left[(1+3\cos^2\theta)K_I^2 + 8\sin\theta\cos\theta K_I K_{II}\right.\\ &\left.+(9-5\cos^2\theta)K_{II}^2\right].\end{aligned} \tag{8}$$

Then the crack initiation angle θ_0 is obtained from

$$\partial\mathcal{G}(\theta)/\partial\theta = 0, \quad \partial^2\mathcal{G}(\theta)/\partial\theta^2 < 0 \Rightarrow \theta = \theta_0. \tag{9}$$

Once the crack initiation angle is determined, the crack initiation condition is given by

$$\mathcal{G}(\theta_0) = \mathcal{G}_c(x), \tag{10}$$

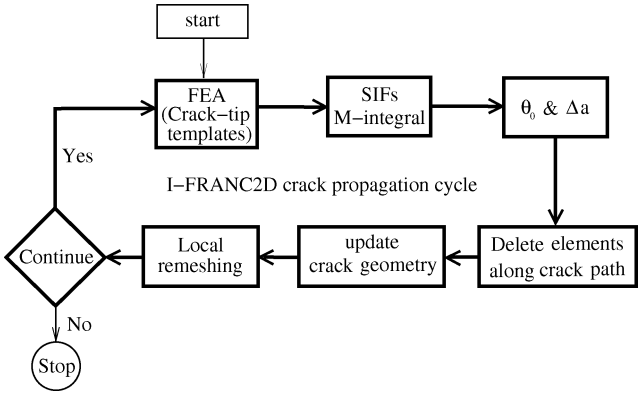

FIG. 5. I-FRANC2D automatic crack propagation algorithm for FGMs.

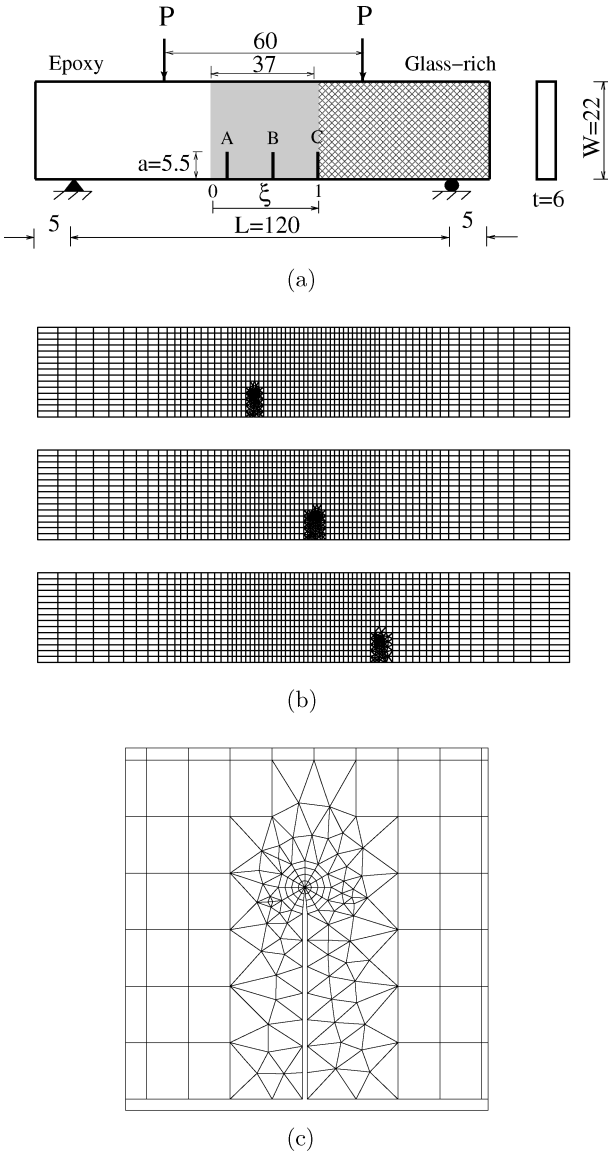

FIG. 6. Example 1: A crack in a graded glass/epoxy beam subjected to four-point bending: (a) geometry, boundary conditions, and three independent cracks A ($\xi = 0.17$), B ($\xi = 0.58$) and C ($\xi = 1.00$) (Units: N, mm); (b) the complete mesh configurations for cracks A, B, and C; (c) mesh detail using 12 sectors (S12) and 4 rings (R4) around the crack tip.

where $\mathcal{G}_c(x)$ is the critical energy release rate function given by

$$\mathcal{G}_c(x) = \frac{K_{Ic}^2(x)}{E^*_{\text{tip}}} \tag{11}$$

2.3. Minimum Strain Energy Density

Sih [39] proposed the minimum strain energy density criterion for homogeneous materials. The local strain energy density is given by [39]

$$\frac{dW}{dA} = \frac{1}{r}S, \tag{12}$$

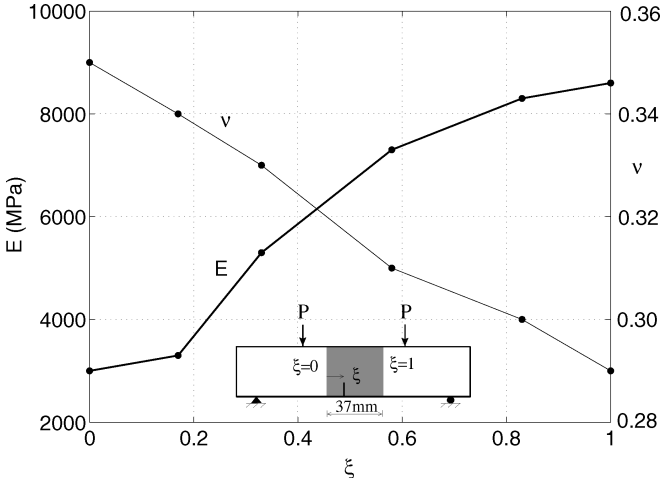

FIG. 7. Example 1: Variations of Young's modulus E (MPa) and Poisson's ratio ν along the graded region ($0 \le \xi \le 1$).

where dA is the volume of the differential element $dA = r\,d\theta\,dr$, and S is the strain energy density factor given by [39]

$$S = d_{11}K_I^2 + 2d_{12}K_IK_{II} + d_{22}K_{II}^2, \tag{13}$$

where the parameters d_{ij} are functions of the angle θ given by [39]

$$\begin{aligned} d_{11} &= \frac{1}{16\mu_{\text{tip}}\pi}(1+\cos\theta)(\kappa_{\text{tip}} - \cos\theta), \\ d_{12} &= \frac{1}{16\mu_{\text{tip}}\pi}\sin\theta(2\cos\theta - \kappa_{\text{tip}} + 1), \\ d_{22} &= \frac{1}{16\mu_{\text{tip}}\pi}[(\kappa_{\text{tip}}+1)(1-\cos\theta) \\ &\quad + (1+\cos\theta)(3\cos\theta - 1)]. \end{aligned} \tag{14}$$

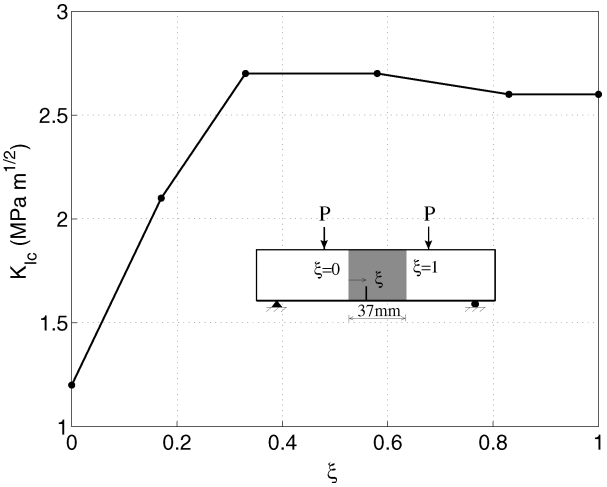

FIG. 8. Example 1: Variation of fracture toughness K_{Ic} (MPa $\sqrt{m}$) along the graded region ($0 \le \xi \le 1$).

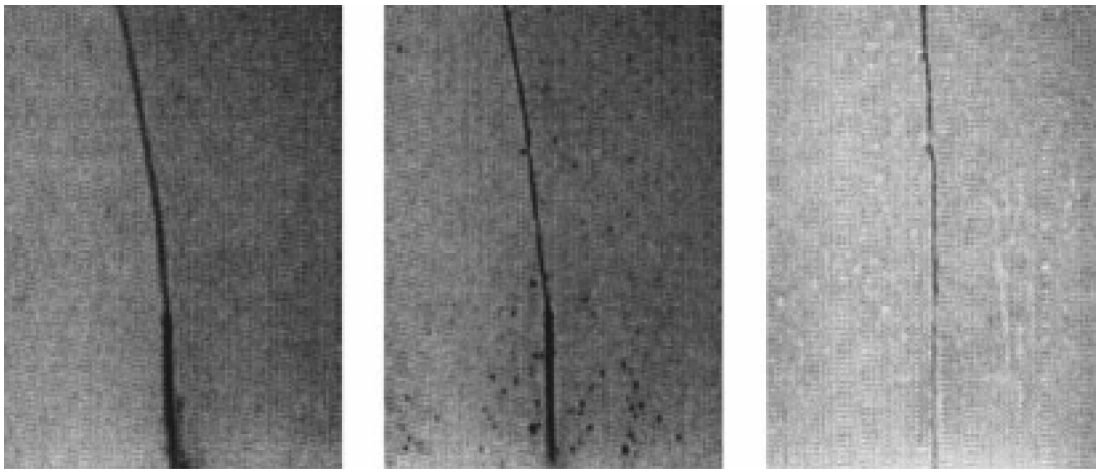

(a) ξ=0.17 ($\theta_0 = 7^\circ$) (b) ξ=0.58 ($\theta_0 = 4^\circ$) (c) ξ=1.00 ($\theta_0 = 0.5^\circ$)

FIG. 9. Example 1: Experimental results for crack trajectories and crack initiation angles (θ_0) of the crack in an FGM beam reported by Rousseau and Tippur [23]: (a) $\xi = 0.17$; (b) $\xi = 0.58$; (c) $\xi = 1.00$.

The criterion postulates that the crack will grow in the direction where S is the minimum. Therefore the crack initiation angle θ_0 is obtained as

$$\partial \mathcal{S}(\theta) = 0, \quad \partial^2 \mathcal{S}(\theta)/\partial \theta^2 > 0 \quad \Rightarrow \quad \theta = \theta_0. \tag{15}$$

Once the crack initiation angle is determined, the crack initiation condition is given by

$$\mathcal{S}(\theta_0) = \mathcal{S}_c(\boldsymbol{x}), \tag{16}$$

where $\mathcal{S}_c(\boldsymbol{x})$ is the critical strain energy density factor given by

$$\mathcal{S}_c(\boldsymbol{x}) = \frac{\kappa_{\text{tip}} - 1}{8\mu_{\text{tip}}} \mathrm{K}_{\mathrm{IC}}^2(\boldsymbol{x}). \tag{17}$$

3. STRATEGY FOR AUTOMATIC CRACK PROPAGATION

Crack propagation in FGMs is performed by means of the I-FRANC2D (Illinois-FRANC2D) code. The code is based on the FRANC2D (FRacture ANalysis Code 2D) [50, 51], which was originally developed at Cornell University. The extended capabilities of I-FRANC2D consist of graded elements to discretize nonhomogeneous materials (see Figure 4), and fracture parameters such as SIFs for predicting crack initiation angle and determining crack growth in FGMs. The computer code uses quarter-point six-node triangular (T6qp) elements to capture the stress singularity of $O(r^{-1/2})$, and it controls mesh refinement around the crack tip in both radial (rings) and hoop (sectors)

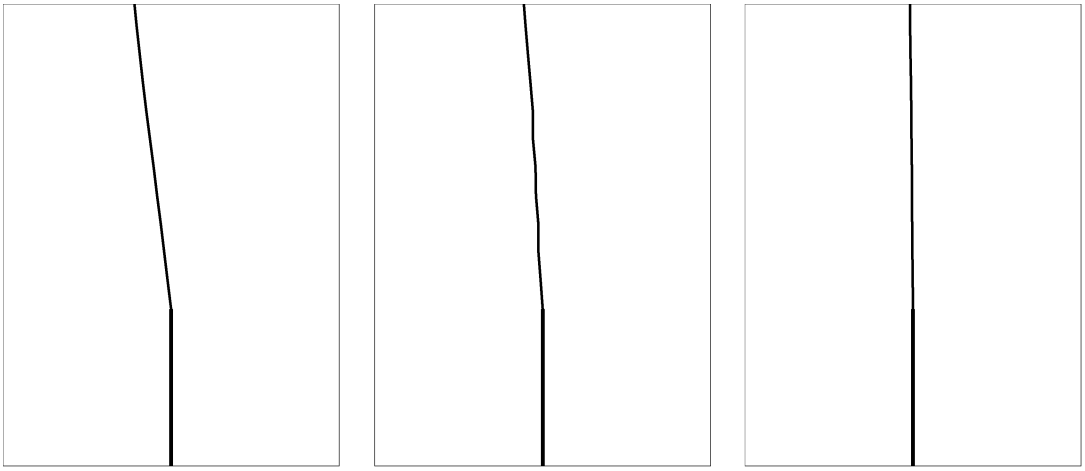

(a) ξ=0.17 ($\theta_0 = 6.98^\circ$) (b) ξ=0.58 ($\theta_0 = 4.01^\circ$) (c) ξ=1.00 ($\theta_0 = 0.59^\circ$)

FIG. 10. Example 1: Numerical results for crack trajectories and crack initiation angles (θ_0) of the crack in an FGM beam (($\sigma_{\theta\theta})_{\max}$ criterion): (a) $\xi = 0.17$; (b) $\xi = 0.58$; (c) $\xi = 1.00$.

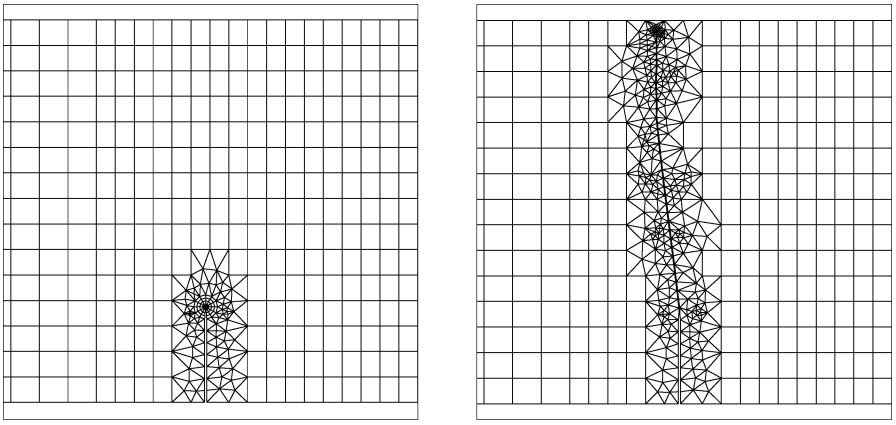

(a) Initial step (b) Final step

FIG. 11. Example 1: finite element discretization and remeshing during crack propagation considering $\xi = 0.17$ and $\Delta a = 1$ mm ($(\sigma_{\theta\theta})_{\max}$ criterion): (a) Initial step; (b) Final step (Step 16).

directions during crack propagation (see Figure 4). This capability allows the definition of crack-tip templates for the local mesh [28].

Finite element simulation of automatic crack propagation in the I-FRANC2D code involves a series of steps. Each step involves an automatic crack propagation cycle as illustrated in Figure 5. The I-FRANC2D code utilizes a direct stiffness FEM approach within the framework of linear elasticity. After the linear finite element analysis involving a crack, the code computes mixed-mode SIFs using the interaction integral method [49, 52–54]. The computed SIFs are used to predict crack growth direction based on fracture criteria (e.g., maximum hoop stress, maximum energy release rate, or minimum strain energy density criteria) . The SIFs and fracture toughness are used to determine crack growth condition. When the new crack tip location is determined according to the user-defined crack increment, the code deletes elements along the incremental crack path, updates crack geometry, and performs automatic local remeshing. The details on crack propagation procedures for homogeneous materials and remeshing schemes are found in [55].

4. THE INTERACTION INTEGRAL: STRESS INTENSITY FACTORS

The interaction integral (M-integral[1]) method is an accurate scheme to evaluate stress intensity factors in FGMs [49, 52–54]. The auxiliary fields and the relationship between SIFs and M-integral are explained below.

[1]Here, the so-called M-integral should not be confused with the M-integral (conservation integral) of Knowles and Sternberg [56], Budiansky and Rice [57], and Chang and Chien [58]. Also, see the book by Kanninen and Popelar [59] for a review of conservation integrals in fracture mechanics.

The interaction integral uses auxiliary fields, such as displacements ($\boldsymbol{u}^{aux}$), strains ($\boldsymbol{\varepsilon}^{aux}$), and stresses ($\boldsymbol{\sigma}^{aux}$) suitable for mixed-mode SIFs. There are various choices for the auxiliary fields for FGMs. Here a non-equilibrium formulation is adopted, which uses displacement and strain fields developed for homogeneous materials, and employs the non-equilibrium stress fields given by [49, 60]

$$\boldsymbol{\sigma}^{aux} = \boldsymbol{C}(\boldsymbol{x})\boldsymbol{\varepsilon}^{aux}, \tag{18}$$

where $\boldsymbol{C}(\boldsymbol{x})$ is the stiffness tensor. The auxiliary displacement, strain and stress fields are chosen as [61]:

$$\boldsymbol{u}^{aux} = \frac{K_I^{aux}}{\mu_{\text{tip}}}\sqrt{\frac{r}{2\pi}}\boldsymbol{g}^{I}(\theta) + \frac{K_{II}^{aux}}{\mu_{\text{tip}}}\sqrt{\frac{r}{2\pi}}\boldsymbol{g}^{II}(\theta), \tag{19}$$

$$\boldsymbol{\varepsilon}^{aux} = (\text{sym}\nabla)\boldsymbol{u}^{aux}, \tag{20}$$

where K_I^{aux} and K_{II}^{aux} are the auxiliary mode I and mode II SIFs, respectively, and μ_{tip} is the shear modulus at the crack tip. The representative functions $\boldsymbol{g}^{I}(\theta)$ and $\boldsymbol{g}^{II}(\theta)$ can be found in many references, e.g., [62].

The interaction integral is derived from the path-independent J-integral [63] for two admissible states (actual and auxiliary) of a cracked elastic FGM body and it is given by [49]

$$M = \int_A \left\{\sigma_{ij}u_{i,1}^{aux} + \sigma_{ij}^{aux}u_{i,1} - \sigma_{ik}\varepsilon_{ik}^{aux}\delta_{1j}\right\}q,_j\, dA + \int_A \left\{\underline{\sigma_{ij,j}^{aux}u_{i,1}} - C_{ijkl,1}\varepsilon_{kl}\epsilon_{ij}^{aux}\right\} q\, dA, \tag{21}$$

where the underlined term is a non-equilibrium term, which appears due to non-equilibrium of the auxiliary stress fields,

and must be considered to obtain converged path-independent solutions. The last term is due to material nonhomogeneity and involves the material gradient.

The relationship between J-integral and the mode I and mode II SIFs is given by

$$J_{\text{local}} = \left(K_I^2 + K_{II}^2\right)/E^*_{\text{tip}}, \tag{22}$$

where $E^*_{\text{tip}} = E_{\text{tip}}$ for plane stress and $E_{\text{tip}}/(1-\nu^2_{\text{tip}})$ for plane strain. For two admissible fields, which are the actual ($\boldsymbol{u}$, $\boldsymbol{\varepsilon}$, $\boldsymbol{\sigma}$) and auxiliary ($\boldsymbol{u}^{aux}$, $\boldsymbol{\varepsilon}^{aux}$, $\boldsymbol{\sigma}^{aux}$) fields, one obtains [64]

$$J^s_{\text{local}} = \frac{\left(K_I + K_I^{aux}\right)^2 + \left(K_{II} + K_{II}^{aux}\right)^2}{E^*_{\text{tip}}} = J_{\text{local}} + J^{aux}_{\text{local}} + M_{\text{local}}, \tag{23}$$

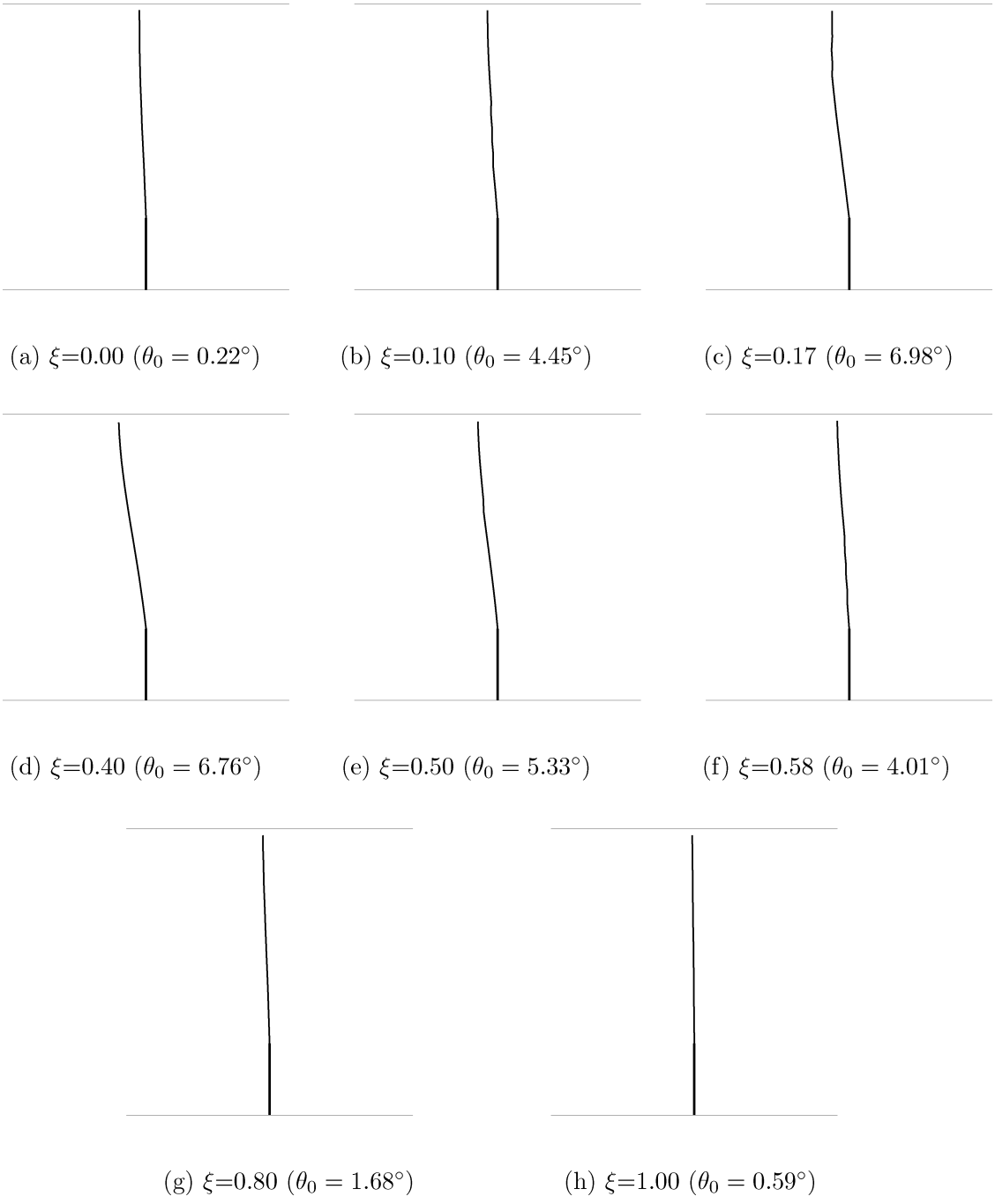

(a) ξ=0.00 ($\theta_0 = 0.22°$) (b) ξ=0.10 ($\theta_0 = 4.45°$) (c) ξ=0.17 ($\theta_0 = 6.98°$)

(d) ξ=0.40 ($\theta_0 = 6.76°$) (e) ξ=0.50 ($\theta_0 = 5.33°$) (f) ξ=0.58 ($\theta_0 = 4.01°$)

(g) ξ=0.80 ($\theta_0 = 1.68°$) (h) ξ=1.00 ($\theta_0 = 0.59°$)

FIG. 12. Example 1: Numerical results for crack trajectories and crack initiation angles (θ_0) of the crack in an FGM beam considering $\Delta a = 1$ mm for all the steps ($(\sigma_{\theta\theta})_{\max}$ criterion): (a) $\xi = 0.00$; (b) $\xi = 0.10$; (c) $\xi = 0.17$; (d) $\xi = 0.40$; (e) $\xi = 0.50$; (f) $\xi = 0.58$; (g) $\xi = 0.80$; (h) $\xi = 1.00$.

where J_{local} is given by Eq. (22), J_{local}^{aux} is given by

$$J_{\text{local}}^{aux} = \left[\left(K_I^{aux}\right)^2 + \left(K_{II}^{aux}\right)^2\right]/E_{\text{tip}}^* \tag{24}$$

and M_{local} is given by

$$M_{\text{local}} = 2\left(K_I K_I^{aux} + K_{II} K_{II}^{aux}\right)/E_{\text{tip}}^*. \tag{25}$$

The mode I and mode II SIFs are evaluated as follows:

$$K_I = M_{\text{local}}^{(1)} E_{\text{tip}}^*/2, \quad \left(K_I^{aux} = 1.0, K_{II}^{aux} = 0.0\right), \tag{26}$$

$$K_{II} = M_{\text{local}}^{(2)} E_{\text{tip}}^*/2, \quad \left(K_I^{aux} = 0.0, K_{II}^{aux} = 1.0\right). \tag{27}$$

The relationships of Eqs. (26) and (27) are the same as those for homogeneous materials [64] except that, for FGMs, the material properties are evaluated at the crack-tip location [53, 65, 66].

5. NUMERICAL EXAMPLES

Fracture analysis and crack propagation are conducted using the FEM code I-FRANC2D. The geometry is discretized with isoparametric graded elements [67]. The specific elements used in the numerical simulations consist of singular quarter-point six-node triangles (T6qp) for crack-tip discretization, eight-node serendipity elements (Q8) for a circular region around crack-tip elements, and regular six-node triangles (T6) in a transition zone of Q8 elements. For the calculation of SIFs by means of the interaction integral, we use a crack-tip region discretization involving 12 sectors (S12) and 4 rings (R4) at each step of crack propagation as recommended by Kim and Paulino [53]. This discretization defines the invariant crack tip template. Quasi-static automatic mixed-mode crack propagation in FGMs are performed in the following examples:

(1) A crack in a graded glass/epoxy beam subjected to four-point bending
(2) Two cracks emanating from holes in a plate under tension
(3) Branched cracks in a plate under tension

In order to validate the numerical results, we adopt the experimental data reported by Rousseau and Tippur [23]. The first example involves mixed-mode crack propagation in a graded glass/epoxy beam [23] under four-point loading. The second example involves two cracks emanating from holes in a plate under tension. The last example involves two branched cracks in a plate under tension and it is motivated by the crack branching phenomenon [68–70].

5.1. A Crack in a Graded Glass/Epoxy Beam Subjected to Four-Point Bending

Rousseau and Tippur [23] investigated crack growth behavior of a crack normal to the material gradient in a graded glass/epoxy subjected to four-point bending, and applied displacement controlled loading at a cross-head speed of 0.25 mm/min using Instron Universal Testing Machine. The FGM beam was made of solid A-glass spheres of mean diameter 42 μm dispersed within a slow curing epoxy matrix, and was fabricated by using gravity assisted casting technique with two-part slow curing epoxy and uncoated solid glass sphere fillers.

Figure 6(a) shows specimen geometry and boundary conditions (BCs) considering three independent cracks A, B, and C, which are located at $\xi = 0.17$, 0.58, and 1.00, respectively, Figure 6(b) shows the complete mesh configurations for the three

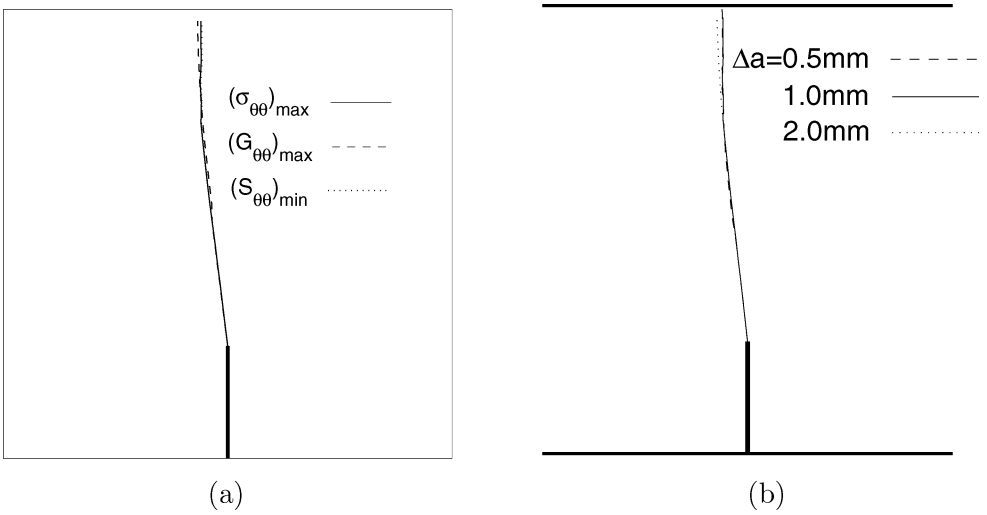

FIG. 13. Example 1: (a) comparison of crack trajectories obtained by using the maximum hoop stress [36], maximum energy release rate [37], and minimum strain energy density [39] criteria. The crack initiation angles at the initial step obtained by $(\sigma_{\theta\theta})_{\max}$, $(\mathcal{G}_{\theta\theta})_{\max}$, and $(\mathcal{S}_{\theta\theta})_{\min}$ are $\theta_0 = 6.98^\circ$, 6.98°, and 7.64°, respectively; (b) sensitivity of the crack trajectory with respect to the crack increment Δa, and comparison of solutions obtained with $\Delta a = 0.5$ mm, 1.0 mm, and 2.0 mm using the maximum hoop stress criterion.

cracks, and Figure 6(c) shows mesh detail using 12 sectors (S12) and 4 rings (R4) around the crack tip.

The typical mesh discretization consists of 1067 Q8, 155 T6, and 12 T6qp elements, with a total of 1234 elements and 3725 nodes. The following data are used for the FEM analyses:

$$\text{plane stress},$$
$$\text{a/W} = 0.25, \quad \text{t} = 6\ \text{mm}, \quad \text{P} = \text{P}_{cr}(a + n\Delta a, \boldsymbol{X}). \quad (28)$$

where n refers to the number of crack propagation increments, and $\boldsymbol{X} = (X_1, X_2)$.

Figures 7 and 8 illustrate variations of Young's modulus E and Poisson's ratio ν and fracture toughness K_{Ic} in the graded material region, respectively. The numerical values of material properties at interior points in the graded region are illustrated in Table 1.

Due to the lack of information on the critical load P_{cr} and load history in [23], here the critical load is calculated at each step based on fracture criteria, and applied the calculated critical load to the corresponding step. Notice that there is no effect of the load magnitude on the crack trajectory within the framework of linear elastic analysis. Table 2 shows the critical load P_{cr}, SIFs,

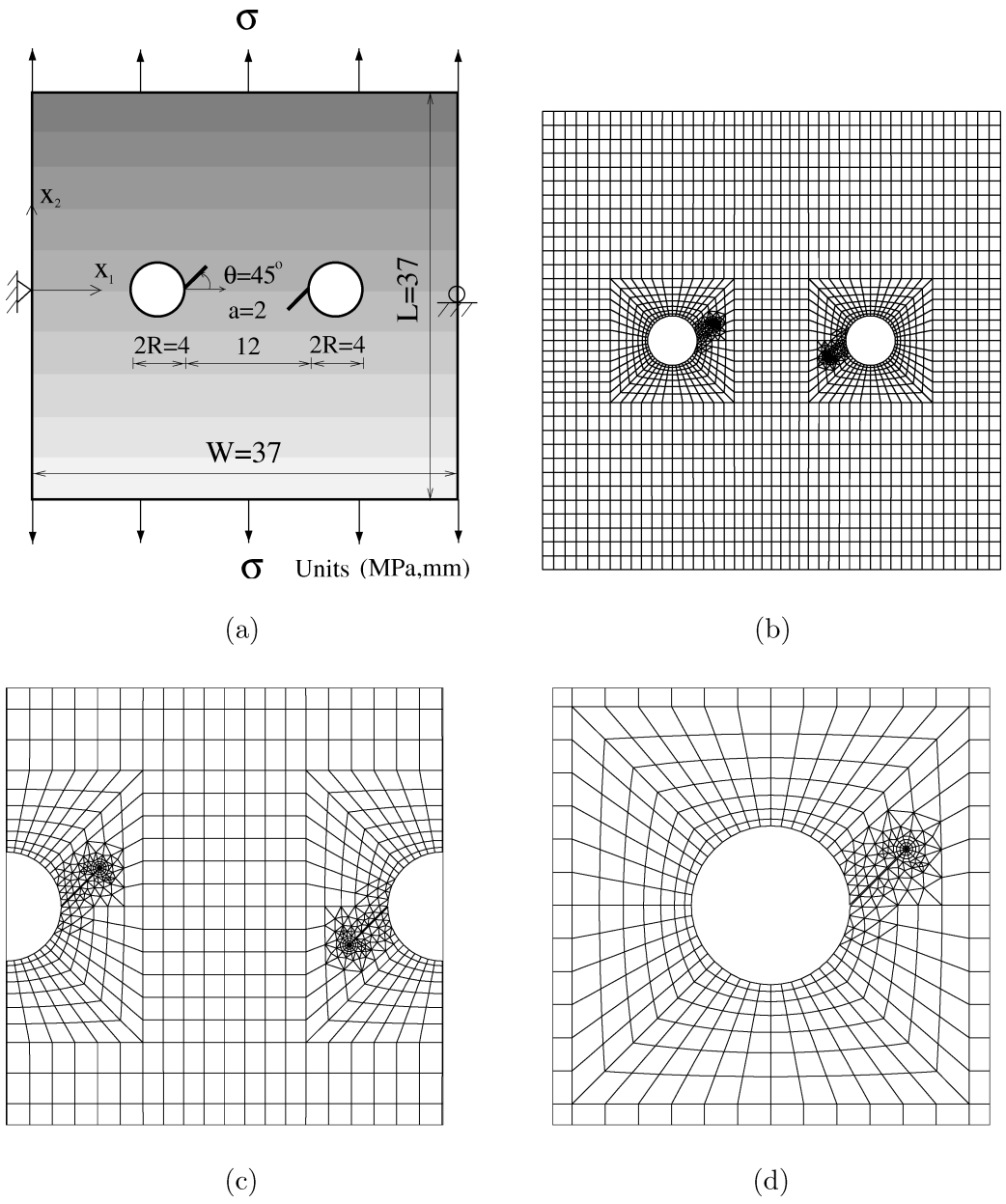

FIG. 14. Example 2: An FGM plate with two cracks emanating from holes: (a) geometry and BCs; (b) complete finite element mesh; (c) mesh details of two crack tips; (d) zoom of the left crack tip showing mesh of 12 sectors (S12) and 4 rings (R4) elements.

TABLE 1
Example 1: Material properties (Young's modulus E, Poisson's ratio ν, and fracture toughness K_{Ic}) at interior points in the graded region

ξ	E(MPa)	ν	K_{Ic} (MPa $\sqrt{m}$)
0.00	3000	0.35	1.2
0.17	3300	0.34	2.1
0.33	5300	0.33	2.7
0.58	7300	0.31	2.7
0.83	8300	0.30	2.6
1.00	8600	0.29	2.6

and the phase angle $\psi = \tan^{-1}(K_{II}/K_I)$ calculated using the maximum hoop stress criterion at the initial step considering the three crack locations $\xi = 0.17$, 0.58, and 1.00. As ξ increases, the mode-mixity K_I/K_{II} decreases.

Figures 9(a), 9(b), and 9(c) show experimental results reported by Rousseau and Tippur [23] for crack trajectories and crack initiation angles (θ_0) of the crack located at $\xi = 0.17$, $\xi = 0.58$, and $\xi = 1.00$, respectively. Figures 10(a), 10(b), and 10(c) show present numerical results for crack trajectories and crack initiation angles (θ_0) for the corresponding cracks. These numerical results are obtained by considering the maximum hoop stress criterion [36] and a crack increment $\Delta a = 1$ mm. There is reasonable agreement in crack initiation angles and crack trajectories between numerical and experimental results. Figure 11 shows finite element discretization and remeshing for initial, intermediate and final steps of crack propagation considering the crack located at $\xi = 0.17$ and $\Delta a = 1$ mm. One can observe that local mesh is refined around the crack tip at each step.

In order to investigate the effect of initial crack location on crack trajectory, cracks located at various locations in a graded beam are considered. Figure 12 shows numerical results for crack trajectories and crack initiation angles (θ_0) considering various crack locations ($0 \le \xi \le 1$) and $\Delta a = 1$ mm. Notice that, as the crack location changes from $\xi = 0.0$ to $\xi = 1.0$, the crack initiation angle θ_0 increases up to about 6.98° at $\xi = 0.17$, and then decreases. For homogeneous beam with the crack $\xi = 0.5$, the crack initiation angle is zero because of symmetry, but, for a graded beam investigated here, it is nonzero.

TABLE 2
Example 1: Numerical results for the critical load P_{cr}, SIFs, and phase angle $\psi = \tan^{-1}(K_{II}/K_I)$) at the initial step considering the three crack locations: $\xi = 0.17$, 0.58, and 1.00. ($(\sigma_{\theta\theta})_{\max}$ criterion)

ξ	P_{cr} (N)	K_I (MPa $\sqrt{m}$)	K_{II} (MPa $\sqrt{m}$)	$\psi = \tan^{-1}(K_{II}/K_I)$
0.17	249.3	2.088	−0.127	−3.480
0.58	298.0	2.695	−0.094	−1.997
1.00	289.9	2.598	−0.013	−0.286

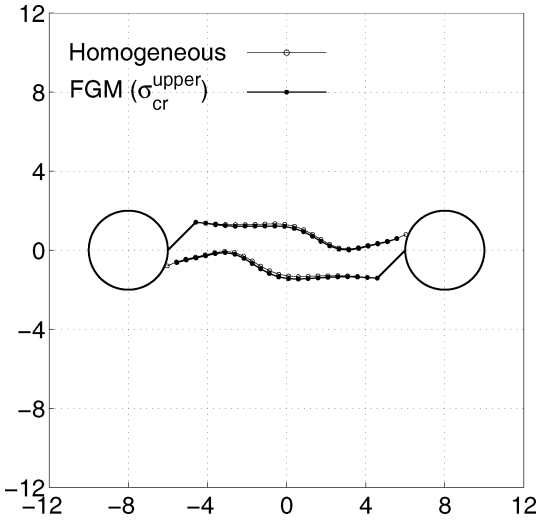

FIG. 15. Example 2: comparison of crack trajectories between homogeneous and graded plates. For a graded plate, the upper-limit load, which is required for both cracks to propagate, is considered for each step of crack propagation ($(\mathcal{G}_{\theta\theta})_{\max}$ criterion, $\Delta a = 0.5$ mm).

In order to compare the three fracture criteria, i.e., $(\sigma_{\theta\theta})_{\max}$, $(\mathcal{G}_{\theta\theta})_{\max}$, and $(\mathcal{S}_{\theta\theta})_{\max}$ criteria, Figure 13(a) shows crack trajectories obtained by using the maximum hoop stress [36], the maximum energy release rate [37], and the minimum strain energy density [39] criteria. There is not much difference in crack trajectories. Moreover, the crack initiation angles at the initial step obtained by maximum hoop stress [36], minimum strain energy density [39], and maximum energy release rates [37]

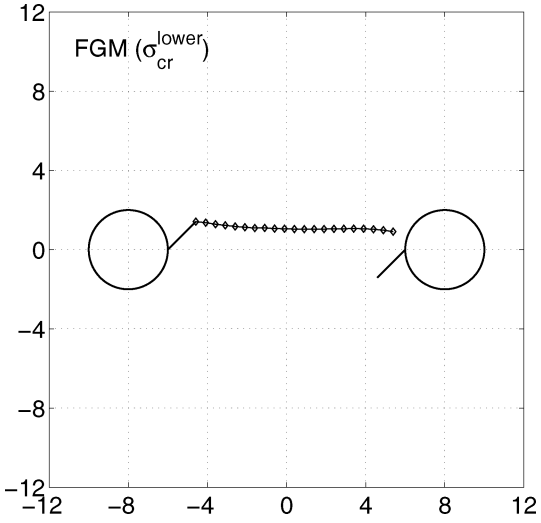

FIG. 16. Example 2: crack trajectory for cracks in a graded plate. The lower-limit load, which is required for the crack with higher crack driving force to propagate, is considered for each step of crack propagation ($(\mathcal{G}_{\theta\theta})_{\max}$ criterion, $\Delta a = 0.5$ mm).

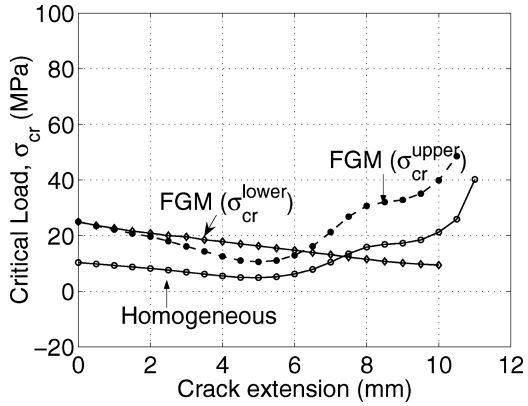

FIG. 17. Example 2: critical load (σ_{cr}) versus crack extension history for homogeneous and graded plates (($\mathcal{G}_{\theta\theta}$)$_{\max}$ criterion, $\Delta a = 0.5$ mm).

criteria are $\theta_0 = 6.98^\circ$, $\theta_0 = 6.98^\circ$, and $\theta_0 = 7.64^\circ$, respectively. To investigate the effect of the crack increment Δa on crack trajectory, Figure 13(b) shows comparison of crack trajectories obtained by considering $\Delta a = 0.5$ mm, 1.0 mm, and 2.0 mm and using the maximum hoop stress criterion. There is not much difference in the crack trajectory for the crack increments Δa considered here. However, inappropriate large values of the crack increment may lead to accumulative deviation of crack trajectory.

5.2. Two Cracks Emanating from Holes in a Plate under Tension

This example investigates the interaction of two cracks emanating from holes in a plate. Figure 14(a) shows specimen geometry and BCs; Figure 14(b) shows the complete mesh configuration; Figure 14(c) shows mesh detail of two cracks; and Figure 14(d) shows zoom of the left crack tip region showing mesh of 12 sectors (S12) and 4 rings (R4) elements.

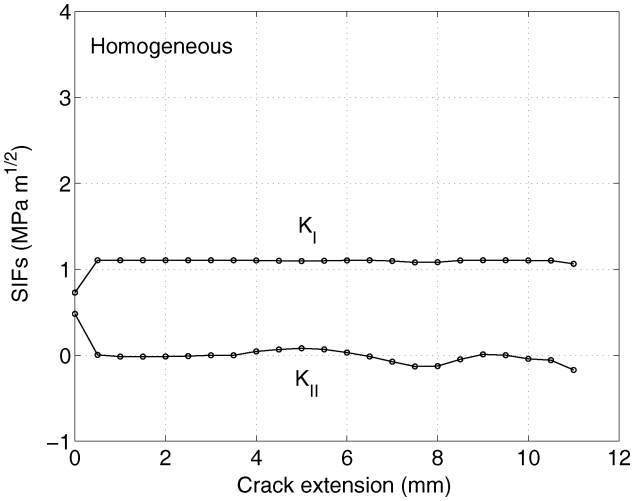

FIG. 18. Example 2: History of SIFs (K_I and K_{II} versus crack extension for the homogeneous plate (($\mathcal{G}_{\theta\theta}$)$_{\max}$ criterion, $\Delta a = 0.5$ mm).

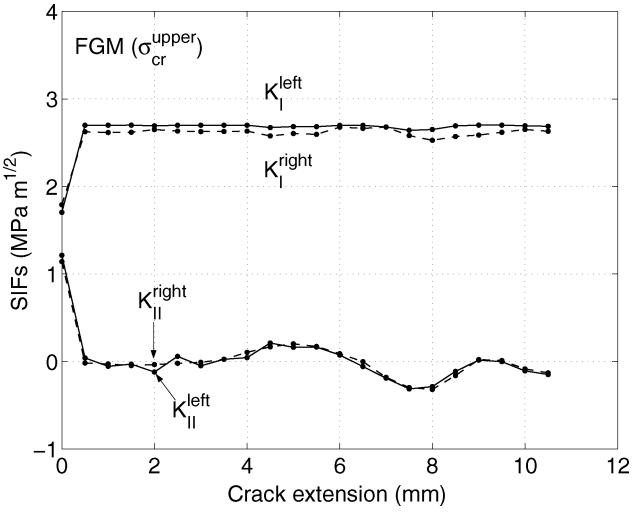

FIG. 19. Example 2: History of SIFs (K_I and K_{II}) versus crack extension for the graded plate considering the upper-limit load (($\mathcal{G}_{\theta\theta}$)$_{\max}$ criterion, $\Delta a = 0.5$ mm).

The typical mesh discretization consists of 1964 Q8, 302 T6, and 24 T6qp elements, with a total of 2290 elements and 6827 nodes. The following data are used for the FEM analyses:

$$\text{plane stress,}$$
$$\text{a} = 2 \text{ mm}, \quad \text{t} = 6 \text{ mm}, \quad \sigma = \sigma_{cr}(a + n\Delta a, \boldsymbol{X}) \text{ (MPa)}. \tag{29}$$

Here material properties are adopted from the first example. For the homogeneous beam, the material properties of epoxy are used (see Table 1). For the graded beam, material gradation in the X_2 direction is considered, and the graded region -18.5 mm $\le X_2 \le 18.5$ mm corresponds to the graded region $0 \le \xi \le 1$ in the first example (cf. Figures 7 and 8).

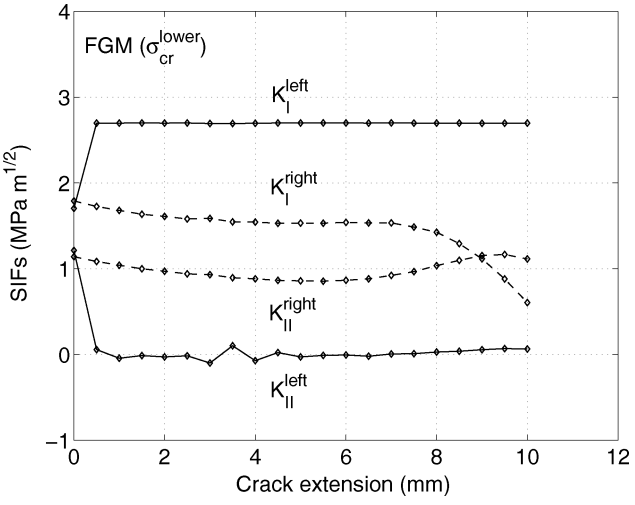

FIG. 20. Example 2: History of SIFs (K_I and K_{II}) versus crack extension for the graded plate considering the lower-limit load (($\mathcal{G}$)$_{\max}$ criterion, $\Delta a = 0.5$ mm).

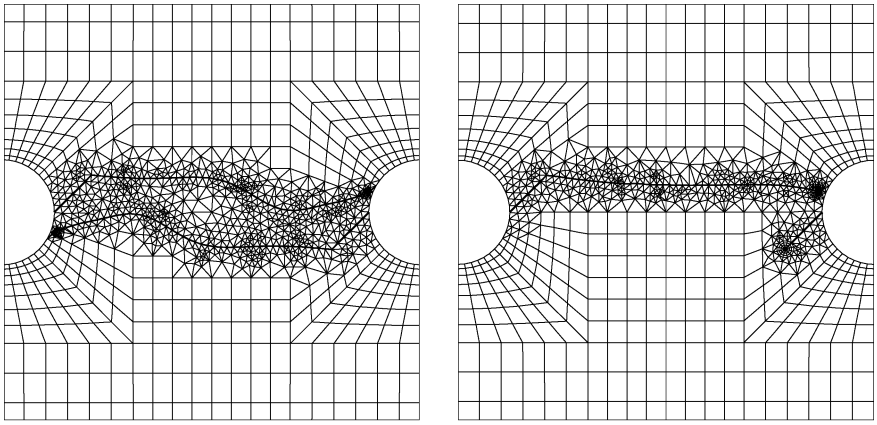

FIG. 21. Example 2: finite element discretization in the final step of crack propagation considering $\Delta a = 0.5$ mm (($\mathcal{G}_{\theta\theta})_{\max}$ criterion): (a) Homogeneous case; (b) the lower-limit load of FGM case. The final discretization of the upper-limit load case is similar to that for the homogeneous case, and thus is not shown here.

Figure 15 shows comparison of crack trajectories obtained for the homogeneous plate with those for the graded plate using the maximum energy release rates criterion [37]. For the homogeneous plate, crack trajectories for the left and right crack tips are symmetric. For the graded plate, the upper-limit load ($\sigma_{cr}^{\text{upper}}$), which is required for both cracks to propagate, is considered for each step of crack propagation ($\Delta a = 0.5$ mm). Due to material gradation, two cracks propagate toward the compliant part of graded plate, and the symmetry breaks down.

Figure 16 shows crack trajectories obtained by using the maximum energy release rates criterion [37] for the graded plate considering the lower-limit load ($\sigma_{cr}^{\text{lower}}$) at each step, which is required for the crack with higher crack driving force to propagate. As observed in Figure 16, only the left crack propagates and the right crack is shielded. This indicates that the crack driving force of the left crack is higher than that for the right crack for the entire step of crack propagation.

Figure 17 shows history of critical load (σ_{cr}) versus crack extension for homogeneous and graded plates ($\Delta a = 0.5$ mm) using the maximum energy release rates criterion [37]. Due to higher fracture toughness in FGMs, the critical load at the initial step for the graded plate is higher than that for the homogeneous case. The critical load considering lower-limit case of the graded plate decreases with the increasing steps. However, the critical load considering the upper-limit case of the graded plate decreases up to step 10 (crack extension 5 mm) due to the interaction between two cracks and increases thereafter, which is also observed in the homogeneous case.

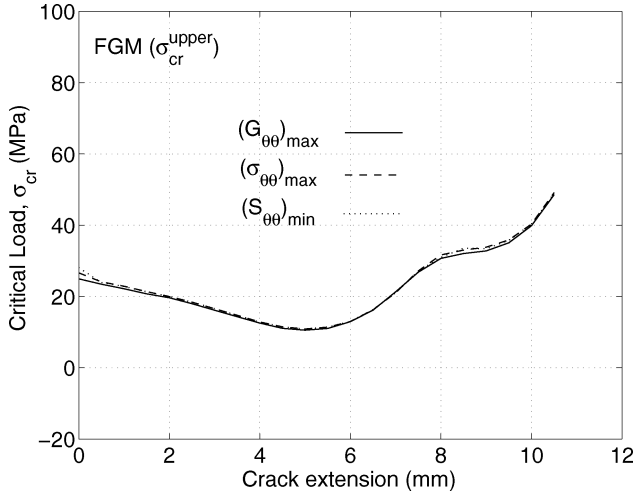

FIG. 22. Example 2: Comparison of critical load histories obtained using $(\mathcal{G}_{\theta\theta})_{\max}$, $(\sigma_{\theta\theta})_{\max}$, and $(\mathcal{S}_{\theta\theta})_{\min}$ criteria for the upper-limit load case of FGMs.

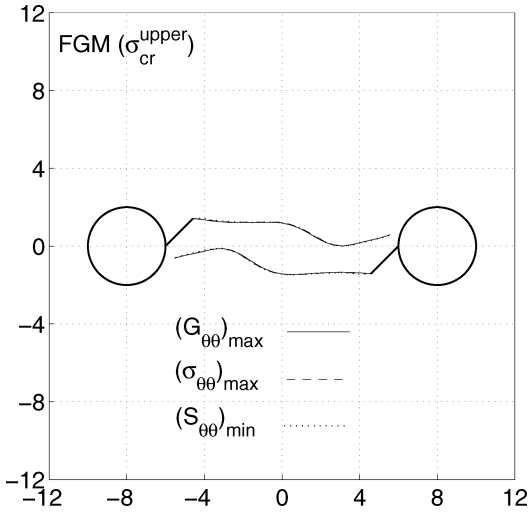

FIG. 23. Example 2: Comparison of crack trajectories obtained using $(\mathcal{G}_{\theta\theta})_{\max}$, $(\sigma_{\theta\theta})_{\max}$, and $(\mathcal{S}_{\theta\theta})_{\min}$ criteria for the upper-limit load case of FGMs.

Figure 18 shows history of SIFs K_I and K_{II} versus crack extension for the homogeneous plate ($\Delta a = 0.5$ mm) using the maximum energy release rates criterion [37]. The SIFs for both crack tips are identical because of symmetry. Figures 19 and 20 show history of SIFs (K_I and K_{II}) versus crack extension for the graded plates considering the upper-limit and lower-limit loads, respectively. For both upper and lower limit load cases, due to higher fracture toughness and subsequent increased critical loads, one observes increased mode I SIF for both crack tips. Moreover, for the lower-limit load case, as observed in Figure 16, the right crack tip does not propagate, and mode II SIF for the right crack tip is positive. For both homogeneous and graded materials, crack grows such that K_{II} tend to oscillate around zero (i.e., $K_{II} = 0$ criterion).

Figure 21 shows finite element discretization in the final step of crack propagation considering $\Delta a = 0.5$ mm for the homogeneous case and the lower-limit load of FGM case, respectively. The final discretization of upper-limit load case is similar to that for the homogeneous case, and thus is not shown here.

Figures 22 and 23 compare critical load histories and crack trajectories, respectively, obtained using $(\mathcal{G}_{\theta\theta})_{\max}$, $(\sigma_{\theta\theta})_{\max}$, and $(S_{\theta\theta})_{\min}$ criteria for the upper-limit load case of FGMs. There is

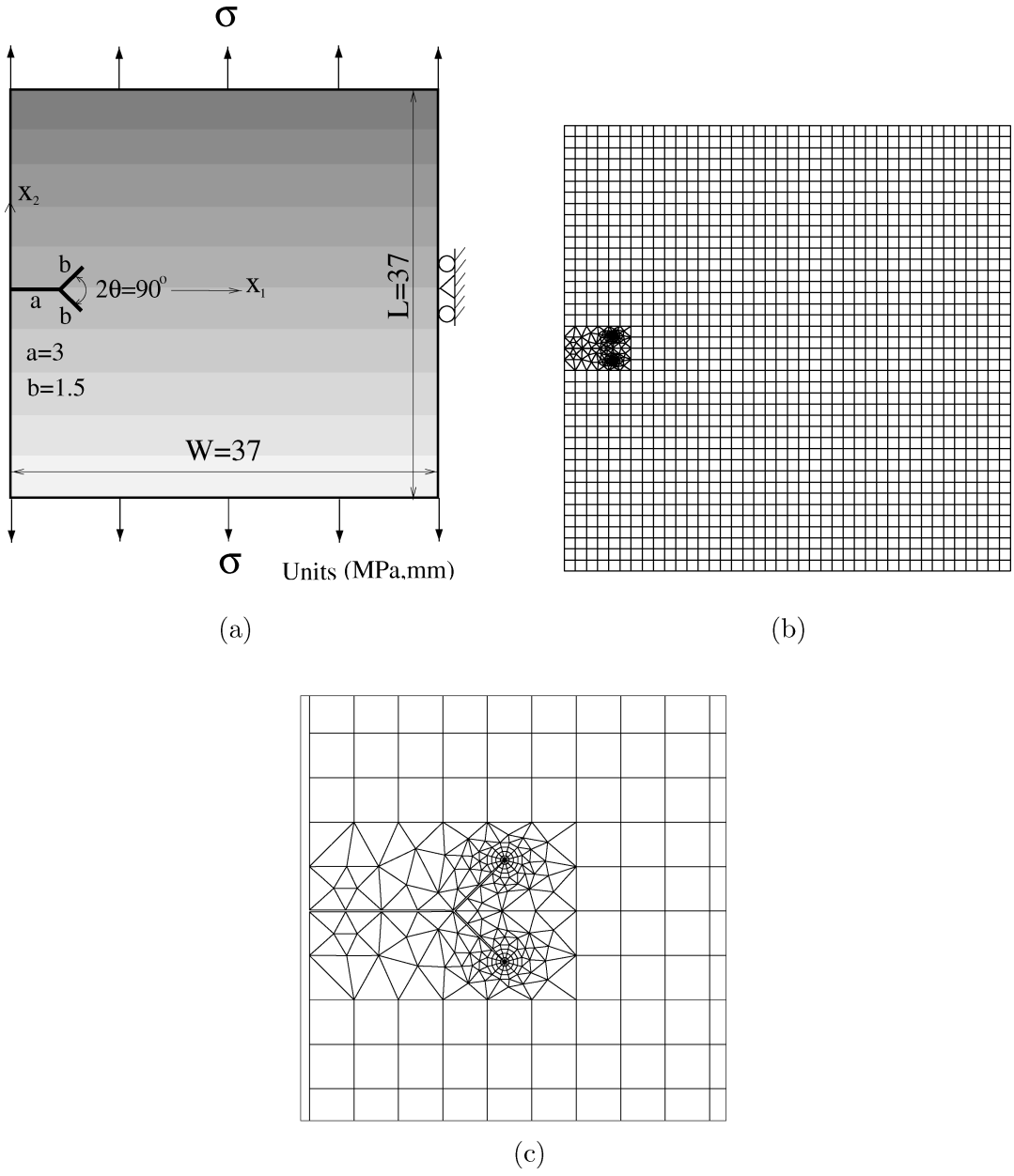

FIG. 24. Example 3: An FGM plate with branched cracks: (a) geometry and BCs; (b) complete finite element mesh; (c) mesh details using 12 sectors (S12) and 4 rings (R4) elements.

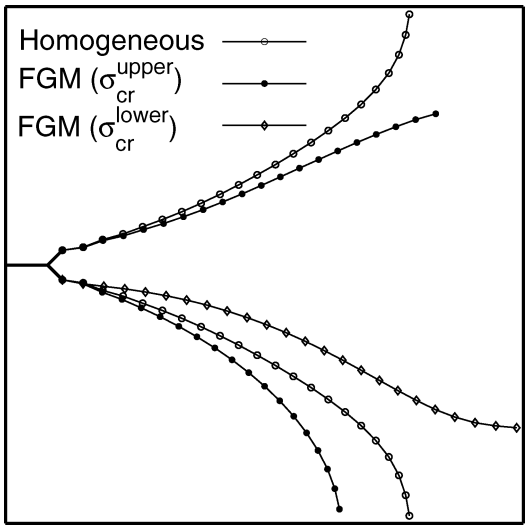

FIG. 25. Example 3: comparison of crack trajectories between homogeneous and graded plates ($(\mathcal{G}_{\theta\theta})_{\max}$ criterion, $\Delta a = 1.5$ mm).

not much difference in critical load history and crack trajectory calculated by using the three fracture criteria.

5.3. Branched Cracks in a Plate under Tension

This example investigates branched cracks extending from the existing crack tip. Figure 24(a) shows specimen geometry and BCs; Figure 24(b) shows the complete mesh configuration; and Figure 24(c) shows mesh detail of forked cracks using 12 sectors (S12) and 4 rings (R4) elements.

The typical mesh discretization consists of 1644 Q8, 212 T6, and 24 T6qp elements, with a total of 1880 elements and 5605

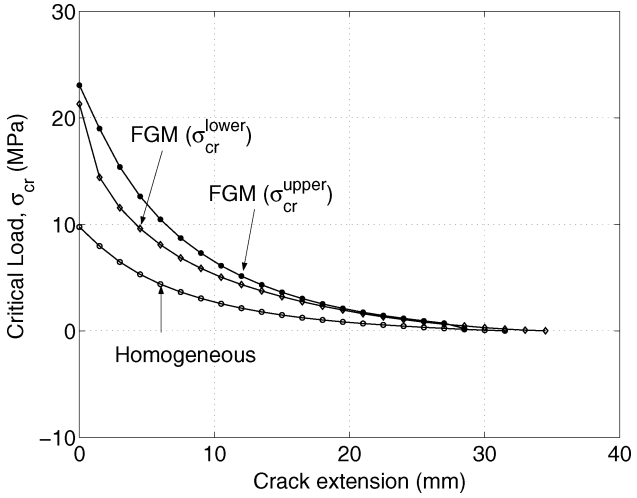

FIG. 26. Example 3: History of critical load (σcr) versus crack extension for homogeneous and graded plates ($(\mathcal{G}_{\theta\theta})_{\max}$ criterion, $\Delta a = 1.5$ mm).

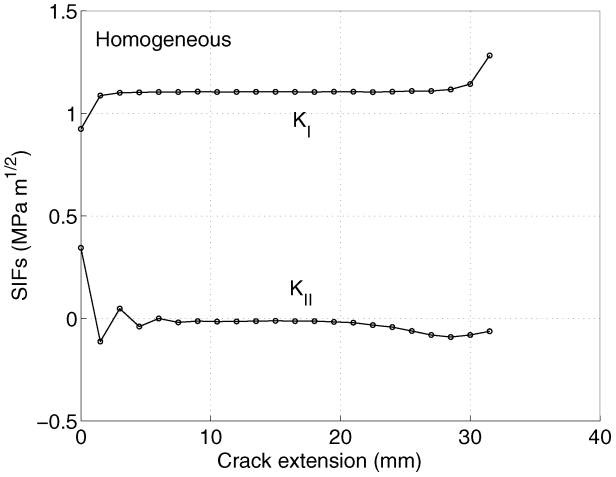

FIG. 27. Example 3: History of SIFs (K_I and K_{II}) versus crack extension for the homogeneous plate ($(\mathcal{G}_{\theta\theta})_{\max}$ criterion, $\Delta a = 1.5$ mm).

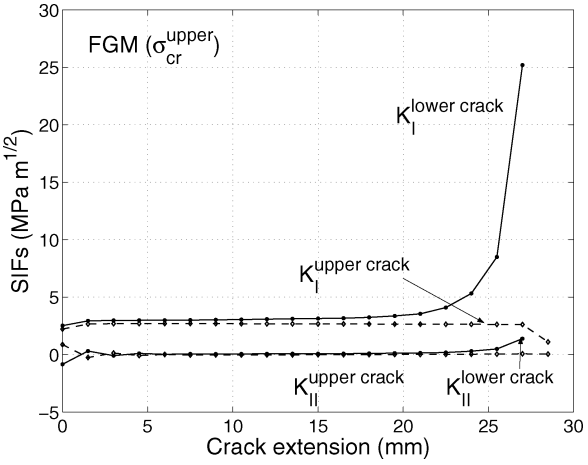

FIG. 28. Example 3: History of SIFs (K_I and K_{II}) versus crack extension for the graded plate considering the upper-limit load ($(\mathcal{G}_{\theta\theta})_{\max}$ criterion, $\Delta a = 1.5$ mm).

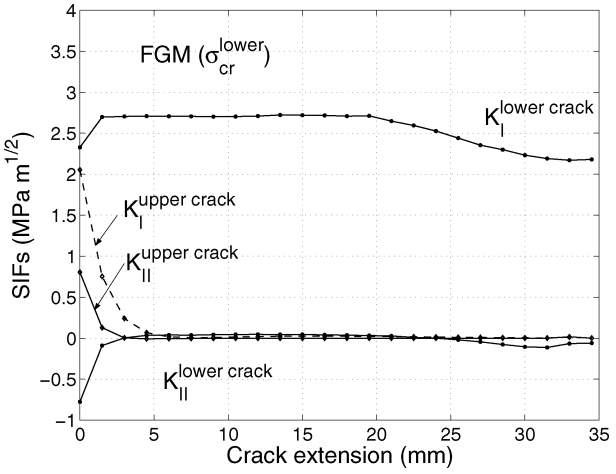

FIG. 29. Example 3: History of SIFs (K_I and K_{II}) versus crack extension for the graded plate considering the lower-limit load ($(\mathcal{G}_{\theta\theta})_{\max}$ criterion, $\Delta a = 1.5$ mm).

nodes. The following data are used for the FEM analyses:

$$\begin{aligned} &\text{plane stress,}\\ &\text{a} = 3 \text{ mm}, \quad \text{b} = 1.5 \text{ mm}, \quad \text{t} = 6 \text{ mm},\\ &\sigma = \sigma_{cr}(a + n\Delta a, \boldsymbol{X}) \text{ (MPa)}. \end{aligned} \tag{30}$$

Here again material properties are adopted from the first example, and the material gradation is identical to the second example. For the homogeneous beam, the material properties of epoxy are used (see Table 1). For the graded beam, material gradation in the X_2 direction is considered, and the graded region $-18.5 \text{ mm} \leq X_2 \leq 18.5 \text{ mm}$ corresponds to the graded region $0 \leq \xi \leq 1$ in the first example (cf. Figures 7 and 8).

Figure 25 shows comparison of crack trajectories obtained for the homogeneous plate with those for the graded plate ($\Delta a = 1.5$ mm) using the maximum energy release rates criterion [37]. As observed for the upper-limit load in the previous example, due to material gradation, two cracks propagate toward the compliant part of graded plate, and the symmetry breaks down. As observed for the lower-limit load case in Figure 25, only the lower crack propagates and the upper crack is shielded. This indicates that the crack driving force of the lower crack is higher than that for the upper crack for the entire step of crack propagation.

Figure 26 shows history of critical load (σ_{cr}) versus crack extension for homogeneous and graded plates ($\Delta a = 1.5$ mm) using the maximum energy release rates criterion [37]. Due to higher fracture toughness in FGMs, the critical load for the

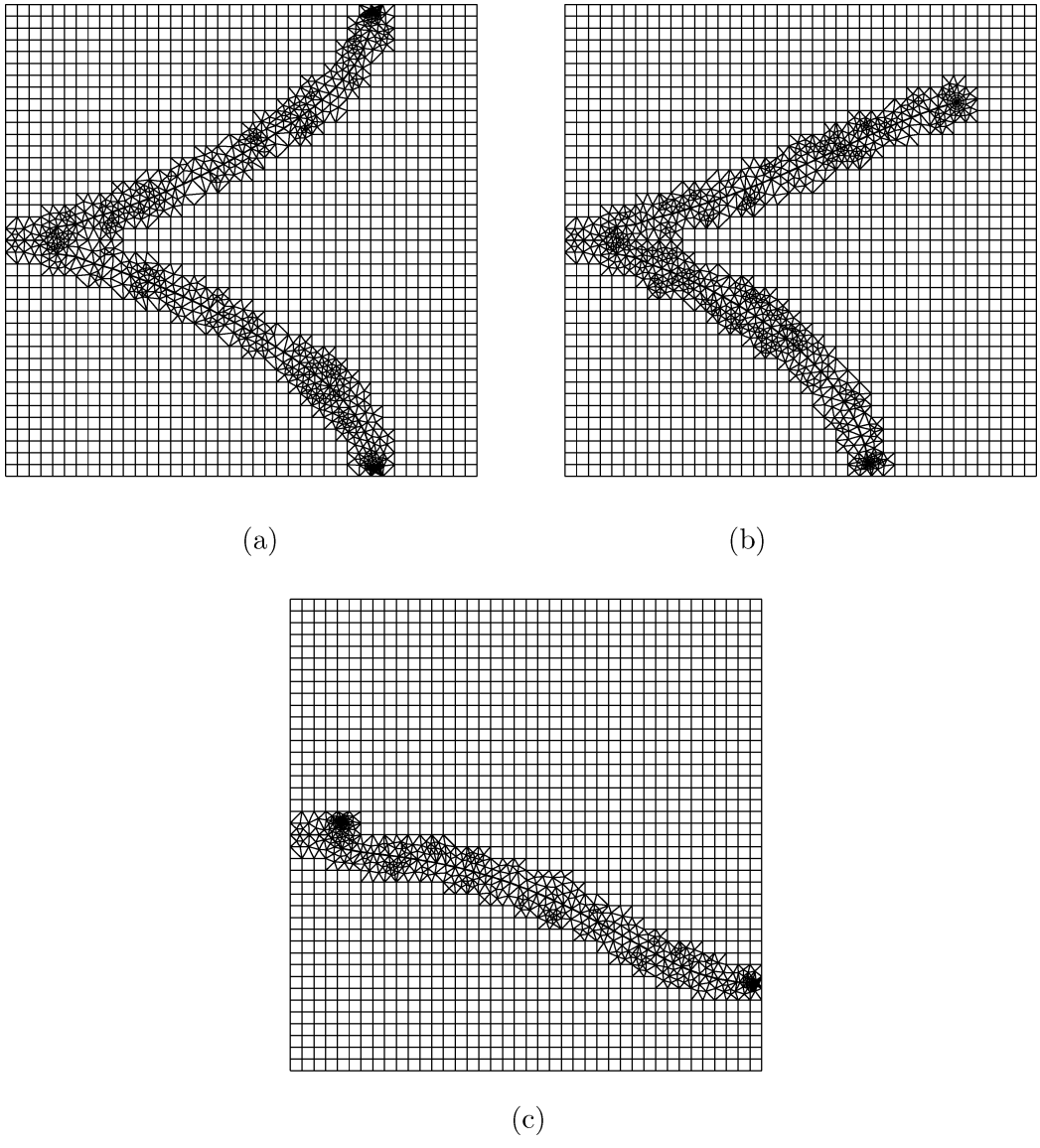

FIG. 30. Example 3: finite element discretization in the final step of crack propagation considering $\Delta a = 0.5$ mm for forked cracks ($(\mathcal{G}_{\theta\theta})_{\max}$ criterion): (a) Homogeneous case; (b) the upper-limit load of FGM case; (c) the lower-limit load of FGM case.

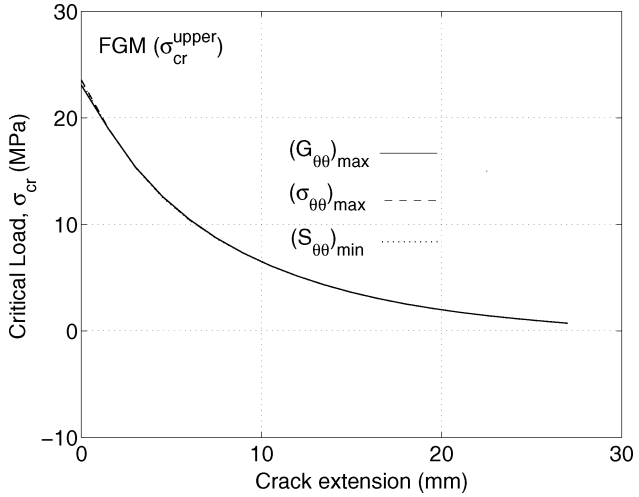

FIG. 31. Example 3: Comparison of critical load histories obtained using $(\mathcal{G}_{\theta\theta})_{\max}$, $(\sigma_{\theta\theta})_{\max}$, and $((\mathcal{S}_{\theta\theta})_{\min}$ criteria for the upper-limit load case of FGMs.

graded plate at each step is higher than that for the homogeneous case. One observes that the critical loads for all cases decrease with each step of propagation.

Figure 27 shows history of SIFs K_I and K_{II} versus crack extension for the homogeneous plate ($\Delta a = 1.5$ mm) using the maximum energy release rates criterion [37]. The SIFs for both crack tips are identical because of symmetry. Figures 28 and 29 show history of SIFs K_I and K_{II} versus crack extension for the graded plates considering the upper-limit and lower-limit loads, respectively. For both upper and lower limit load cases, due to higher fracture toughness and subsequent increased critical loads, one observes increased mode I SIF for both crack tips. Moreover, for the upper-limit load case, as observed in Figure 28, mode I SIF for the lower crack tip increases rapidly at the final step because it is near to the boundary. For the lower-limit load case, as observed in Figure 29, the upper crack tip does not propagate, and both mode I and II SIFs for the upper crack tip rapidly decreases at the early steps. Figure 30 shows finite element discretization in the final step of crack propagation considering $\Delta a = 1.5$ mm for the homogeneous case, the upper-limit and the lower-limit loads of FGM case, respectively.

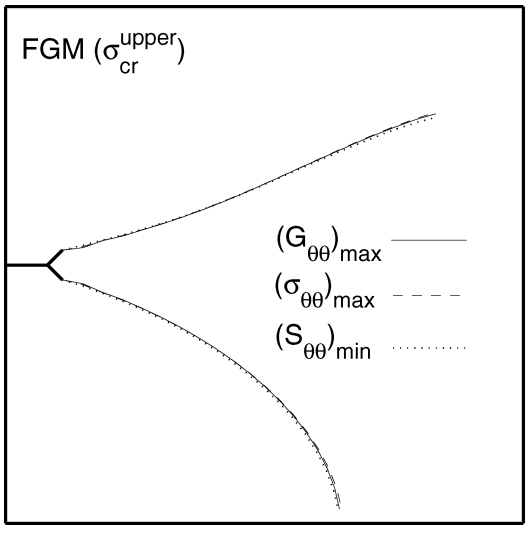

FIG. 32. Example 3: Comparison of crack trajectories obtained using $(\mathcal{G}_{\theta\theta})_{\max}$, $(\sigma_{\theta\theta})_{\max}$, and $((\mathcal{S}_{\theta\theta})_{\min}$ criteria for the upper-limit load case of FGMs.

Figures 31 and 32 compare critical load histories and crack trajectories, respectively, obtained using $(\mathcal{G}_{\theta\theta})_{\max}$, $(\sigma_{\theta\theta})_{\max}$, and $(S_{\theta\theta})_{\min}$ criteria for the upper-limit load case of FGMs. As observed before, there is not much difference in critical load history and crack trajectory calculated by using the three fracture criteria.

6. CONCLUSIONS

This paper investigates mixed-mode fracture behavior of FGMs by performing automatic simulation of crack propagation by means of the finite element method. Based on local homogenization, the maximum hoop stress [36], maximum energy release rate [37] and minimum strain energy [39] criteria are used, and predict crack initiation angles well in comparison with experimental results [23]. Crack trajectories obtained by the three fracture criteria are similar to each other for the considered crack growth examples, and agree well with available experimental results for homogeneous and FGMs.

For two interacting cracks under symmetry boundary conditions, there exists symmetry in terms of fracture parameters characterizing crack-tip fields and crack growth behavior, and thus there is no competition between two cracks for homogeneous materials. However, for graded materials, the symmetry breaks down due to material gradation, and thus the crack-tip fields in one crack tip is different from those for the other. This may allow propagation of one crack and shielding of the other crack under certain critical loads, which range in between the critical loads for the two crack tips.

The present approach uses user-defined crack increment that is specified at the beginning of simulation. The crack increment is related to material behavior, and need be thoroughly investigated with experiments.

ACKNOWLEDGEMENTS

We would like to thank the support from NASA-Ames, Engineering for Complex Systems Program, and the NASA-Ames Chief Engineer (Dr. Tina Panontin) through grant NAG 2-1424. Additional support from the National Science Foundation (NSF) under grant CMS-0115954 (Mechanics & Materials Program) is also appreciated. The first author acknowledges the start-up support from the University of Connecticut. Any opinions expressed herein are those of the writers and do not necessarily reflect the views of the sponsors.

REFERENCES

1. Hirai, T., "Functionally gradient materials and nanocomposites," In: J. B. Holt, M. Koizumi, T. Hirai, and Z. A. Munir (Eds.), *Proceedings of the Second International Symposium on Functionally Gradient Materials*, *Ceramic Transactions*, Vol. 34, 11–20, Westerville, Ohio. The American Ceramic Society (1993).
2. Suresh, S., and Mortensen, A. *Fundamentals of Functionally Graded Materials*. IOM Communications Ltd, London (1998).
3. Paulino, G. H., Jin, Z. H., and Dodds, Jr., R. H., "Failure of functionally graded materials," In: B. Karihaloo and W. G. Knauss (Eds.), *Comprehensive Structural Integrity*, Vol 2, Chap 13. Elsevier Science (2002).
4. Uemura, S., "The activities of FGM on new application," *Materials Science Forum* **423–425**, 1–10 (2003).
5. Hirano, T., Teraki, J., and Yamada, T., "On the design of functionally gradient materials," In: M. Yamanouochi, M. Koizumi, T. Hirai, and I. Shiota (Eds.), *Proceedings of the First International Symposium on Functionally Gradient Materials*, 5–10, Sendai, Japan (1990).
6. Kawasaki, A., and Watanabe, R., "Thermal fracture behavior of metal/ceramic functionally graded biomaterial," *Engineering Fracture Mechanics* **69**, 1713–1728 (2002).
7. Igari, T., Notomi, A., Tsunoda, H., Hida, K., Kotoh, T., and Kunishima, S., "Material properties of functionally gradient material for fast breeder reactor," In: M. Yamanouochi, M. Koizumi, T. Hirai, and I. Shiota (Eds.), *Proceedings of the First International Symposium on Functionally Gradient Materials*, 209–214, Sendai, Japan (1990).
8. Tani, J., and Liu, G. R., "Surface waves in functionally gradient piezoelectric plates," *JSME International Journal Series A (Mechanics and Material Engineering)*, **36**, 152–155 (1993).
9. Hirano, T., Whitlow, L. W., and Miyajima, M., "Numerical analysis of efficiency improvement in functionally gradient thermoelectric materials," In: J. B. Holt, M. Koizumi, T. Hirai, and Z. A. Munir (Eds.), *Proceedings of the Second International Symposium on Functionally Gradient Materials*, *Ceramic Transactions*, Vol. 34, 23–30, Westerville, Ohio. The American Ceramic Society, (1993).
10. Osaka, T., Matsubara, H., Homma, T., Mitamura, S., and Noda, K., "Microstructural study of electroless-plated CoNiReP/NiMoP double-layered media for perpendicular magnetic recording," *Japanese Journal of Applied Physics* **10**, 1939–1943 (1990).
11. Watanabe, Y., Nakamura, Y., Fukui, Y., and Nakanishi, K., "A magnetic-functionally graded material manufactured with deformation-induced martensitic transformation," *Journal of Materials Science Letters* **12**(5), 326–328 (1993).
12. Koike, Y., "Graded-index and single mode polymer optical fibers," In: L. Y. Chiang, A. G. Garito, and D. J. Sandman (Eds.), *Electrical, Optical, and Magnetic Properties of Organic Solid State Materials*, vol. 247, 817, Materials Research Society Proceedings, Pittsburgh, PA (1992).
13. Desplat, J. L., "Recent development on oxigenated thermionic energy converter—overview," In: *Proceedings of the Fourth International Symposium on Functionally Gradient Materials*, Tsukuba City, Japan (1996).
14. Watari, F., Yokoyama, A., Saso, F., Uo, M., Ohkawa, S., and Kawasaki, T., "EPMA elemental mapping of functionally graded dental implant in biocompatibility test," In: *Proceedings of the Fourth International Symposium on Functionally Gradient Materials*, Tsukuba City, Japan (1996).
15. Oonishi, H., Noda, T., Ito, S., Kohda, A., Yamamoto, H., and Tsuji, E., "Effect of hydroxyapatite coating on bone growth into porous titanium alloy implants under loaded conditions," *Journal of Applied Biomaterials* **5**(1), 23–27 (1994).
16. Chu, C., Zhu, J., Yin, Z., and Lin, P., "Structure optimization and properties of hydroxyapatite-Ti symmetrical functionally graded biomaterial," *Materials Science and Engineering A* **361**, 205–210 (2001).
17. Lim, Y.-M., Park, Y.-J., Yun, Y.-H., and Hwang, K.-S., "Functionally graded Ti/HAP coatings on T1-6AL-4V obtained by chemical solution deposition," *Ceramics International* **28**, 37–41 (2002).
18. Getto, H., and Ishihara, S. J., "Development of the fire retardant door with functional gradient wood," In: *Proceedings of the Fourth International Symposium on Functionally Gradient Materials*, Tsukuba City, Japan (1996).
19. Hart, N. T., Brandon, N. P., Day, M. J., and Shemilt, J. E., "Functionally graded cathodes for solid oxide fuel cells," *Journal of Materials Science* **36**, 1077–1085 (2001).
20. Hart, N. T., Brandon, N. P., Day, M. J., and Lapena-Rey, N., "Functionally graded composite cathodes for solid oxide fuel cells," *Journal of Power Sources* **106**, 42–50 (2002).
21. Lin, C. Y., McShane, B., Lin H., and Rawlings, R. D., "Structure and properties of functionally gradient aluminium alloy 2124/sic composites," *Materials Science and Technology* **10**(7), 659–664 (1994).
22. Carpenter, R. D., Liang, W. W., Paulino, G. H., Gibeling, J. C., and Munir, Z. A., "Fracture testing and analysis of a layered functionally graded Ti/TiB beam in 3-point bending," *Materials Science Forum* **308–311**, 837–842 (1999).
23. Rousseau, C.-E., and Tippur, H. V., "Compositionally graded materials with cracks normal to the elastic gradient," *Acta Materialia* **48**(16), 4021–4033 (2000).
24. Lambros, J., Cheeseman, B. A., and Santare, M. H., "Experimental investigation of the quasi-static fracture of functionally graded materials," *International Journal of Solids and Structures* **37**(27), 3715–3732 (2000).
25. Abanto-Bueno, J., and Lambros, J., "Investigation of crack growth in functionally graded materials using digital image correlation," *Engineering Fracture Mechanics* **69**(14–16), 1695–1711 (2002).
26. Jin, Z.-H., Paulino, G. H., and Dodds Jr., R. H., "Finite element investigation of quasi-static crack growth in functionally graded materials using a novel cohesive zone fracture model," *Journal of Applied Mechanics, Transactions ASME* **69**(3), 370–379 (2002).
27. Jin, Z.-H., Paulino, G. H., and Dodds Jr., R. H., "Cohesive fracture modeling of elastic-plastic crack growth in functionally graded materials," *Engineering Fracture Mechanics* **70**, 1885–1912 (2003).
28. Kim, J.-H., and Paulino, G. H., "Simulation of crack propagation in functionally graded materials under mixed-mode and non-proportional loading," *International Journal of Mechanics and Materials in Design* **1**(1):63–94 (2004).
29. Zhang, Z., and Paulino, G. H., "Cohesive zone modeling of dynamic failure in homogeneous and functionally graded materials," *International Journal of Plasticity* 21(6), 1195–1254 (2005).
30. Moon, R. J., Hoffman, M., Hilden, J., Bowman, K. J., Trumble, K. P., and Rodel, J., "R-curve behavior in alumina-zirconia composites with repeating graded layers," *Engineering Fracture Mechanics* **69**(14–16), 1647–1665 (2002).
31. Neubrand, A., Chung, T.-J., and Rodel, J., "Two-cracks propagation problem in a functionally graded material plate under thermal loads," *Materials Science Forum* **423–425**, 607–612 (2003).
32. Fujimoto, T., and Noda, N., "Crack propagation in a functionally graded plate under thermal shock," *Archive of Applied Mechanics* **70**, 377–386 (2000).
33. Noda, N., Ishihara, M., Yamamoto, N., and Fujimoto, T., "Experimental and theoretical investigation of R-curve in Al/Al_2O_3 functionally graded materials," *Materials Science Forum* **423–425**, 269–274 (2003).
34. Uzun, H., Lindley, T. C., McShane, H. B., and Rawlings, R. D., "Fatigue crack growth behavior of 2124/SiC/1Op functionally graded materials," *Metallurgical and Materials Transactions A* **32A**, 1831–1839 (2001).
35. Forth, S. C., Favrow, L. H., Keat, W. D., and Newman, J. A., "Three-dimensional mixed-mode fatigue crack growth in a functionally graded titanium alloy," *Engineering Fracture Mechanics* **70**(15), 2175–2185 (2003).
36. Erdogan, F., and Sih, G. C., "On the crack extension in plates under plane loading and transverse shear," *ASME Journal of Basic Engineering* **85**(4), 519–527 (1963).
37. Hussain, M. A., Pu, S. L., and Underwood, J., "Strain energy release rate for a crack under combined mode I and mode II," In: P. C. Paris and G. R.

Irwin (Eds.), *Fracture Analysis*, ASTM STP 560, 2–28, Philadelphia, PA. American Society for Testing and Materials, (1993).
38. Palaniswamy, K., and Knauss, W. G., "On the problem of crack extension in brittle solids under general loading," in: S. Nemat-Nasser (Ed.), *Mechanics Today*. vol. 4, 87–148, Oxford, Pergamon Press (1978).
39. Sih, G. C., "Strain energy density factor applied to mixed mode crack problems," *International Journal of Fracture* **10**(3), 305–321 (1974).
40. Cotterell, B., and Rice, J. R., "Slightly curved or kinked cracks," *International Journal of Fracture* **16**(2), 155–169 (1980).
41. Theocaris, P. S., and Andrianopoulos, N. P., "The Mises elastic-plastic boundary as the core region in fracture criteria," *Engineering Fracture Mechanics* **16**(3), 425–432 (1982).
42. Kong, X. M., Schluter, N., and Dahl, W., "Effect of triaxial stress on mixed-mode fracture," *Engineering Fracture Mechanics* **52**(2), 379–388 (1995).
43. Wasiluk, B., and Golos, K., "Prediction of crack growth direction under plane stress for mixed-mode I and II loading," *Fatigue and Fracture of Engineering Materials ans Structures* **23**, 381–386 (2000).
44. Golos, K., and Wasiluk, B., "Role of plastic zone in crack growth direction criterion under mixed mode loading," *International Journal of Fracture* **102**, 341–353 (2000).
45. Khan, S. M. A., and Khraisheh, M. K., "A new criterion for mixed mode fracture initiation based on the crack tip plastic core region," *International Journal of Plasticity* **20**(1), 55–84 (2004).
46. Hori, M., and Vaikuntan, N., "Rigorous formulation of crack path in two-dimensional elastic body," *Mechanics of Materials* **26**(1), 1–14 (1997).
47. Fortino, S., and Bilotta, A., "Evaluation of the amount of crack growth in 2D LEFM problems," *Engineering Fracture Mechanics* **71**(9–10), 1403–1419 (2004).
48. Gu, P., and Asaro, R. J., "Crack deflection in functionally graded materials," *International Journal of Solids and Structures* **34**(24), 3085–3098 (1997).
49. Kim, J.-H., and Paulino, G. H., "Consistent formulations of the interaction integral method for fracture of functionally graded materials," *Journal of Applied Mechanics, Transactions ASME* **72**(3), 351–364 (2005).
50. Wawrzynek, P. A., "Interactive finite element analysis of fracture processes: an integrated approach," *M.S. Thesis, Cornell University* (1987).
51. Wawrzynek, P. A., and Ingraffea, A. R., "Discrete modeling of crack propagation: theoretical aspects and implementation issues in two and three dimensions," *Report 91-5, School of Civil Engineering and Environmental Engineering, Cornell University* (1991).
52. Kim, J.-H., and Paulino, G. H., "T-stress, mixed-mode stress intensity factors, and crack initiation angles in functionally graded materials: A unified approach using the interaction integral method," *Computer Methods in Applied Mechanics and Engineering* **192**(11–12), 1463–1494 (2003).
53. Kim, J.-H., and Paulino, G. H., "An accurate scheme for mixed-mode fracture analysis of functionally graded materials using the interaction integral and micromechanics models," *International Journal for Numerical Methods in Engineering* **58**(10), 1457–1497 (2003).
54. Kim, J.-H., and Paulino, G. H., "The interaction integral for fracture of orthotropic functionally graded materials: Evaluation of stress intensity factors," *International Journal of Solids and Structures* **40**(15), 3967–4001 (2003).
55. Bittencourt, T. N., Wawrzynek, P. A., and Ingraffea, A. R., "Quasi-static simulation of crack propagation for 2D LEFM problems," *Engineering Fracture Mechanics* **55**(2), 321–334 (1996).
56. Knowles, J. K., and Sternberg, E., "On a class of conservation laws in linearized and finite elastostatics," *Archive for Rational Mechanics and Analysis* **44**(2), 187–211 (1972).
57. Budiansky, B., and Rice, J. R., "Conservation laws and energy-release rates," *Journal of Applied Mechanics, Transactions ASME* **40**(1), 201–203 (1973).
58. Chang, J. H., and Chien, A. J., "Evaluation of M-integral for anisotropic elastic media with multiple defects," *International Journal of Fracture* **114**(3), 267–289 (2002).
59. Kanninen, M. F., and Popelar, C. H. *Advanced Fracture Mechanics*. Oxford University Press, New York, 1985.
60. Paulino, G. H., and Kim, J.-H., "A new approach to compute T-stress in functionally graded materials using the interaction integral method," *Engineering Fracture Mechanics* **71**(13–14), 1907–1950 (2004).
61. Williams, M. L., "On the stress distribution at the base of a stationary crack," *Journal of Applied Mechanics, Transactions ASME* **24**(1), 109–114 (1957).
62. Eftis, J., Subramonian, N., and Liebowitz, H., "Crack border stress and displacement equations revisited," *Engineering Fracture Mechanics* **9**(1), 189–210 (1977).
63. Rice, J. R., "A path-independent integral and the approximate analysis of strain concentration by notches and cracks," *Journal of Applied Mechanics, Transactions ASME* **35**(2), 379–386 (1968).
64. Yau, J. F., Wang, S. S., and Corten, H. T., "A mixed-mode crack analysis of isotropic solids using conservation laws of elasticity," *Journal of Applied Mechanics, Transactions ASME* **47**(2), 335–341 (1980).
65. Dolbow, J., and Gosz, M., "On the computation of mixed-mode stress intensity factors in functionally graded materials," *International Journal of Solids and Structures* **39**(9), 2557–2574 (2002).
66. Rao, B. N., and Rahman, S., "Mesh-free analysis of cracks in isotropic functionally graded materials," *Engineering Fracture Mechanics* **70**(1), 1–27 (2003).
67. Kim, J.-H., and Paulino, G. H., "Finite element evaluation of mixed-mode stress intensity factors in functionally graded materials," *International Journal for Numerical Methods in Engineering* **53**(8), 1903–1935 (2002).
68. Kitagawa, H., Yuuki, R., and Ohira, T., "Crack-morphological aspects in fracture mechanics," *Engineering Fracture Mechanics* **7**, 515–529 (1975).
69. Lo, K. K., "Analysis of branced cracks," *Journal of Applied Mechanics, Transactions ASME* **45**, 797–802 (1978).
70. Suresh, S., and Shih, C. F., "Plastic near-tip fields for branched cracks," *International Journal of Fracture* **30**, 237–259 (1986).
71. Kim, J.-H., "Mixed-mode crack propagation in functionally graded materials," Ph.D. *Dissertation, Univeristy of Illinois at Urbana-Champagin*, Urbana, IL (2003).